Quantum Monte Carlo study of the phase diagram of the two-dimensional uniform electron liquid

Sam Azadi,[1,*] N. D. Drummond,[2] and Sam M. Vinko[1,3]

[1] *Department of Physics, Clarendon Laboratory, University of Oxford, Parks Road, Oxford OX1 3PU, United Kingdom*

[2] *Department of Physics, Lancaster University, Lancaster LA1 4YB, United Kingdom*

[3] *Central Laser Facility, STFC Rutherford Appleton Laboratory, Didcot OX11 0QX, United Kingdom*

(Dated: December 30, 2024)

We present a study of spin-unpolarized and spin-polarized two-dimensional uniform electron liquids using variational and diffusion quantum Monte Carlo (VMC and DMC) methods with Slater-Jastrow-backflow trial wave functions. Ground-state VMC and DMC energies are obtained in the density range $1 \leq r_s \leq 40$. Single-particle and many-body finite-size errors are corrected using canonical-ensemble twist-averaged boundary conditions and extrapolation of twist-averaged energies to the thermodynamic limit of infinite system size. System-size-dependent errors in Slater-Jastrow-backflow DMC energies caused by partially converged VMC energy minimization calculations are discussed. We find that, for $1 \leq r_s \leq 5$, optimizing the backflow function at each twist lowers the twist-averaged DMC energy at finite system size. However, nonsystematic system-size-dependent effects remain in the DMC energies, which can be partially removed by extrapolation from multiple finite system sizes to infinite system size. The DMC energies in the thermodynamic limit are used to parameterize a local spin density approximation correlation functional for inhomogeneous electron systems. Our zero-temperature phase diagram shows a single transition from a paramagnetic fluid to a hexagonal Wigner crystal at $r_s = 35(1)$, with no region of stability for a ferromagnetic fluid.

I. INTRODUCTION

The uniform electron liquid is one of the most important models in physics which provides a basic understanding of the quantum properties of simple metals and semiconductors and also materials under extreme conditions [1–13]. Determining its ground state properties at a wide range of densities is a challenging problem for many-body methods, because the density controls the strength of the electron-electron interactions and therefore correlations. As the density is lowered and the average distance between electrons increases the Coulomb potential energy decreases as $1/r_s$, where $r_s = (\pi n a_B^2)^{-1/2}$ is the Wigner-Seitz density parameter, n is the density, and $a_B = \hbar^2/(me^2)$ is the Bohr radius. By contrast the average kinetic energy in the low-density regime scales as $r_s^{-\alpha}$, where $\alpha > 1$. In this limit, the kinetic energy becomes much smaller than the Coulomb interaction and consequently the ground state of the system becomes crystal-like, meaning that the ground state wave function (WF) of the electron liquid model can be considered as an antisymmetrized product of localized functions (ultimately δ-functions) located on the positions of a regular lattice. Such a dilute system of electrons represents a prototypical system with strong correlations. The possibility of a crystal phase of the electron liquid was initially suggested by Wigner in 1934 [14]. In an earlier paper, Bloch predicted that spontaneous magnetization occurs in a low-density system of electrons because the exchange interaction energy contribution driven by the alignment of all spins outweighs the kinetic energy [15]. It should be pointed out that the structure of a Wigner crystal cannot be determined *a priori*. Using the classical description of electrostatic energy one can find that the crystal structure with the lowest energy will be the one that, for a given volume of the primitive unit cell, has the first reciprocal lattice vector of the largest magnitude [16]. In two and three dimensions, the crystal structures with this property are the hexagonal and body-centered-cubic lattices, respectively.

An important but challenging question is: at what value of r_s does the transition between uniform electron liquid and the Wigner crystal occur? This is a difficult question to answer because, before the transition, exchange effects play a crucial role and also the system could exist in some form of broken symmetry state such as floating crystal. While perturbation theory cannot be applied to the low-density regime, the early quantum Monte Carlo (QMC) methods yielded a highly accurate description of the phase diagram and crystallization density [17–21]. The phase diagram is obtained by comparing the ground state energies of different phases with different symmetries. One issue of this approach is that the ground state might have a symmetry that was not considered. There are other QMC approaches which try to discover the phase diagram by optimizing the wave function using the variational Monte Carlo (VMC) technique [22, 23]. In this work, we address some of the technical challenges of the QMC approach in calculating the ground-state energy of two-dimensional (2D) uniform electron liquid (UEL) at low densities.

The 2D UEL model which consists of a system of

* sam.azadi@physics.ox.ac.uk

electrons moving in 2D in a uniform, inert, neutralizing background, interacting via the Coulomb potential has been widely studied theoretically [16, 18, 20, 21, 24–29] and can be observed at the interface of metal-oxide-semiconductor structures [30], metal-oxide-semiconductor field-effect transistors [31, 32], quantum wells [32, 33], and MgZnO/ZnO heterostructures [34]. According to the 2D UEL phase diagram reported in Ref. 28, the ground state is a non-spin-polarized (paramagnetic) liquid from high density down to the point of Wigner crystallization. However, in the absence of crystallization, lowering the density would eventually make the paramagnetic fluid phase unstable with respect to a spin-polarized (ferromagnetic) fluid. An experimental study of nonequilibrium transport in low-density 2D electron systems at zero external magnetic field suggests that a fully spin-polarized fluid is stable before crystallization [35], which was also reported by some previous theoretical studies [20, 21]. On the other hand, more recent experimental work has not found a region of stability for the ferromagnetic fluid [34]. At low densities, classical 2D Wigner crystals were produced by spraying electrons onto droplets of liquid He [36], and also quantum 2D Wigner crystals were observed at the interface between two semiconductors [37]. Within the last few decades a wide range of experimental techniques have been deployed to detect the crystallization and appearance of magnetic ordering in low-density 2D electron systems [38–42].

This work revisits the problem of calculating the phase diagram of the 2D UEL by QMC [28]. We improve the trial WF by including additional long-range backflow terms and we look at a broader range of system sizes. The single-particle finite-size (FS) errors of the system at high densities are reduced by optimizing the trial WF at each twist during the twist-averaged calculations. The problem of many-body FS errors, which are traditionally removed using an extrapolation approach, near the crystal-liquid phase transition is discussed in detail. We provide more accurate diffusion quantum Monte Carlo (DMC) ground-state energies at the infinite system size limit, which are used for the parameterization of a correlation functional.

II. DETAILS OF THE QMC CALCULATIONS

We have carried out QMC calculations for 2D UELs with spin polarizations of $\zeta = 0$, 0.5, and 1 within the density range $1 \leq r_s \leq 40$, where r_s is the radius of the circle that contains one electron on average in units of the Bohr radius. We have focused on reducing FS errors [43–46] by using twist-averaging (TA) and extrapolation techniques [17, 18, 47]. We discuss errors in DMC calculations near the crystallization density introduced during WF optimization, whose effects may be exaggerated by FS extrapolation.

Slater-Jastrow-backflow (SJB) WFs [48, 49] with plane-wave orbitals $\exp(i\mathbf{G}\cdot\mathbf{r})$ were used in our QMC calculations for fluid phases. Details of the SJB WF have been explained in our recent studies [50–52]; the principle difference from Ref. 28 is the inclusion of a long-range two-body backflow term $\boldsymbol{\pi}$ that is expanded in a plane-wave basis. This term lowers the variational energy in finite cells and is intended to make the treatment of two-body correlations in different simulation cells more consistent, to aid extrapolation to the thermodynamic limit. We used the variational and diffusion quantum Monte Carlo (VMC and DMC) methods [53] as implemented in the CASINO package [54]. To impose fermionic antisymmetry in our DMC calculations we have used the fixed-node approximation [55], where the nodal surface is forced to be the same as that of the trial WF. The variational parameters in the Jastrow factor and backflow functions were optimized within VMC by minimizing either the energy variance [56, 57] or the mean absolute deviation of the local energies from the median [58], then minimizing the energy expectation value [56, 59]. We used a target population of 2560 walkers in our DMC calculations. At $r_s = 1$, 2, 5, 10, 15, 20, 25, 30, 35, and 40 we used DMC time steps of $\tau = 0.005$, 0.01, 0.05, 1, 1.5, 2, 3, 4, 5, and 6 Ha^{-1}, respectively. Random errors due to TA are larger than the time-step bias in each case.

III. NUMERICAL RESULTS

Our DMC energies obtained at various system sizes using a hexagonal simulation cell are listed in tables I and II. Except where otherwise stated, our Jastrow factors and backflow functions were optimized at zero twist (i.e., pure periodic boundary conditions). For paramagnetic 2D UELs with densities $r_s = 1$, 2, and 5, and system size $N = 146$, we tested separately optimizing the Jastrow factor and backflow function at each twist. The results are listed in Table III. We have used 30 random twists in our analysis. Our analysis shows that separately optimizing the Jastrow factor and backflow function at each twist reduces the TA DMC energy by $-0.225(9)\times10^{-3}/r_s$ Ha/el. for paramagnetic 2D UELs at $N = 146$. These results demonstrate the existence of significant, quasirandom FS errors in TA energies in which the same backflow function is used for all twists.

IV. TRIAL WF OPTIMIZATION

WF optimization [56, 59] is challenging at large system sizes ($N \gtrsim 150$) and at densities near the solid-liquid phase transition ($r_s \gtrsim 20$). Figure 1 shows the energy minimization process for the paramagnetic liquid phase with different system sizes and densities. The SJB WFs used for energy minimization were initially optimized by minimization of the mean absolute deviation (MAD) of the local energies at low densities. The problem of slow convergence with optimization cycle can be observed in Fig. 1. The plots in this figure also show occa-

TABLE I. Twist-averaged diffusion Monte Carlo energy E_{DMC} for N-electron two-dimensional uniform electron liquids with spin polarization $\zeta = 0$ and density parameter r_{s}. SJB WFs were used.

r_{s}	N	E_{DMC} (Ha/el.)	r_{s}	N	E_{DMC} (Ha/el.)
1	146	−0.211457(5)	20	62	−0.046445(1)
1	218	−0.210922(5)	20	110	−0.0464184(8)
1	302	−0.210708(6)	20	146	−0.0464077(8)
...	...	...	20	218	−0.046401(1)
2	146	−0.25901(6)	20	242	−0.046399(1)
2	218	−0.258831(6)	...	...	...
2	302	−0.258665(5)	25	62	−0.0378521(7)
...	...	...	25	110	−0.0378329(4)
5	146	−0.150113(2)	25	146	−0.0378238(5)
5	218	−0.150069(2)	25	254	−0.0378136(5)
5	302	−0.150024(4)	...	...	...
...	...	...	30	62	−0.0319681(9)
10	62	−0.085709(2)	30	170	−0.0319466(5)
10	110	−0.085643(2)	30	254	−0.0319435(4)
10	170	−0.085612(1)	...	...	...
10	302	−0.085582(3)	35	62	−0.0276932(8)
...	...	...	35	122	−0.0276811(3)
15	62	−0.060214(1)	35	254	−0.0276751(7)
15	100	−0.060177(1)	...	...	...
15	170	−0.060160(1)	40	62	−0.0244424(2)
15	242	−0.060148(2)	40	110	−0.0244321(2)
...	...	...	40	146	−0.0244295(2)

TABLE II. As Table I, but for a fully ferromagnetic two-dimensional uniform electron liquid with spin polarization $\zeta = 1$.

r_{s}	N	E_{DMC} (Ha/el.)	r_{s}	N	E_{DMC} (Ha/el.)
1	55	0.124298(6)	20	55	−0.0462735(5)
1	91	0.125157(5)	20	91	−0.0462584(4)
1	169	0.125782(2)	20	139	−0.0462488(2)
...	...	...	20	169	−0.0462449(2)
2	55	−0.195569(3)	...	...	...
2	91	−0.195089(2)	25	55	−0.0377815(4)
2	139	−0.194848(1)	25	91	−0.0377695(4)
2	169	−0.194792(1)	25	139	−0.0377639(2)
...	...	...	25	169	−0.0377603(2)
5	55	−0.143992(2)	...	...	...
5	91	−0.143865(1)	30	55	−0.0319418(3)
5	139	−0.1438037(8)	30	91	−0.0319340(2)
5	169	−0.1437819(5)	30	139	−0.0319296(2)
...	...	...	30	169	−0.0319243(1)
10	55	−0.084688(1)	...	...	...
10	91	−0.0846419(7)	35	55	−0.0276857(3)
10	139	−0.0846251(4)	35	91	−0.0276788(2)
10	169	−0.0846088(4)	35	139	−0.0276739(1)
...	...	...	35	169	−0.0276719(1)
15	55	−0.0597888(9)	...	...	...
15	91	−0.0597629(5)	40	91	−0.0244397(2)
15	139	−0.0597489(4)	40	139	−0.0244353(1)
15	169	−0.0597451(3)	40	169	−0.02443388(9)

sional jumps suggestive of WF parameters moving from one local minimum-energy configuration to another.

Our final WFs are obtained by energy minimization, but usually this requires a reasonable first approximation to the WF, obtained using a different method. Although unreweighted variance minimization exhibits superior numerical stability to energy minimization at high and intermediate densities, we found numerical instabilities in variance minimization for systems with large N and low density. Numerical instability in variance minimization can occur when the nodes of the trial WF are altered during minimization. Near the transition density, we find that numerical instabilities become more severe at large system sizes due to the growth of complexity of the energy landscape in parameter space. Minimizing a more robust measure of the spread of the local energies, such as the MAD [58], provides much lower variational energy (Table IV), because the MAD is less sensitive to divergent local energies [54].

We found that more than a dozen cycles of VMC configuration generation and energy minimization are often required to converge adequately in the regime of large N and large r_{s}, as shown in Fig. 1. The magnitude of the effect is significant on the scale of the FS error, even if the subsequent use of DMC weakens the dependence on the backflow function. A related observation is that

TABLE III. TA DMC energies of paramagnetic 146-electron 2D UELs. The DMC calculations were performed using either the same Jastrow factor and backflow function, optimized at zero twist, for all twists (DMC_0) or SJB WFs separately optimized at each twist (DMC_1).

r_{s}	TA DMC energy (Ha/el.)		Difference (Ha/el.)
	DMC_0	DMC_1	
1	−0.210731(7)	−0.210957(5)	$-0.225(8) \times 10^{-3}$
2	−0.258378(9)	−0.258501(6)	$-0.12(1) \times 10^{-3}$
5	−0.149595(4)	−0.149637(2)	$-0.042(5) \times 10^{-3}$

the TA VMC and DMC energies per particle are often higher than suggested by extrapolation from smaller system sizes (see Figs. 4 and 5).

Residual canonical-ensemble TA errors in the Hartree-Fock (HF) kinetic and exchange energies around the crystallization density are orders of magnitude smaller than the fluctuations in the DMC energy shown in Fig. 5; hence residual momentum quantization effects in the TA energy cannot explain the nonsystematic system-size dependence. Other sources of nonsystematic FS error, such as Ruderman-Kittel oscillations being forced to be commensurate with the simulation cell, may be present in Fig. 4. Such nonsystematic FS errors are at least par-

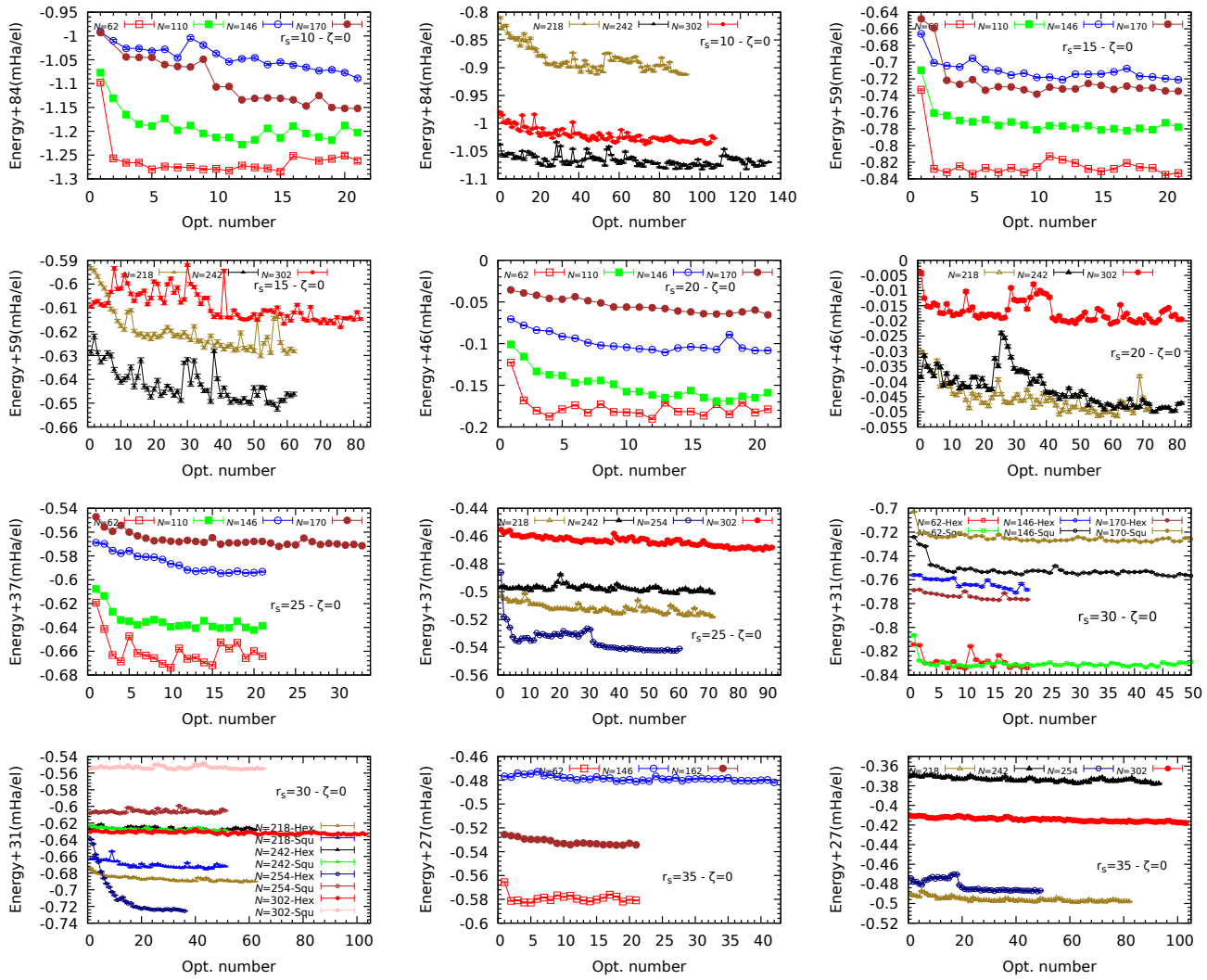

FIG. 1. SJB VMC total energy against energy minimization cycle for different system sizes and density parameters for the paramagnetic 2D UEL at zero twist. The initial WF was optimized by either unreweighted variance minimization or minimization of the MAD from the median local energy.

tially averaged out by extrapolation to the thermodynamic limit.

We investigated this issue further. First, we investigated how the initial SJB WF optimization depends on the number of configurations and the twist. The results are summarized in Table IV. They indicate that the optimized energy for a large system at low density does not depend strongly on the number of configurations or the twist wavevector, but does depend on the optimization method. Because the local energy diverges at nodes, the unreweighted variance and MAD landscapes depend strongly on the sampled configurations. Nevertheless, it is clear that MAD minimization provides much better results than variance minimization and hence better starting points for energy minimization. Second, we compared the FS behavior with Slater-Jastrow (SJ) and SJB WFs. The fixed-node SJ-DMC energy is in principle independent of the Jastrow factor. Figure 4 shows that the TA SJ-DMC energies behave in a nonsystematic manner as a function of system size, and that this behavior is further exaggerated by the inclusion of backflow. This demonstrates (i) that the nonsystematic behavior is not simply a result of difficulties optimizing WFs and (ii) that applying analytic FS corrections [43–45] to results obtained at a single fixed cell size is unreliable because nonsystematic FS effects cannot be removed by this approach. Third, we examined the static structure factor (SF) and momentum density (MD) of a paramagnetic 2D UEL with $N = 254$ at $r_s = 30$ obtained by VMC at a single twist as illustrated in Fig. 2. We have not found significant WF-optimization-dependent or system-size-dependent anomalies in the SF and MD (e.g., the MD retains its discontinuity at the Fermi wavevector).

Fourth, we compared the energies of paramagnetic 2D UELs at $r_s = 30$ obtained using hexagonal and square simulation cells with system sizes $62 \leq N \leq 302$. We

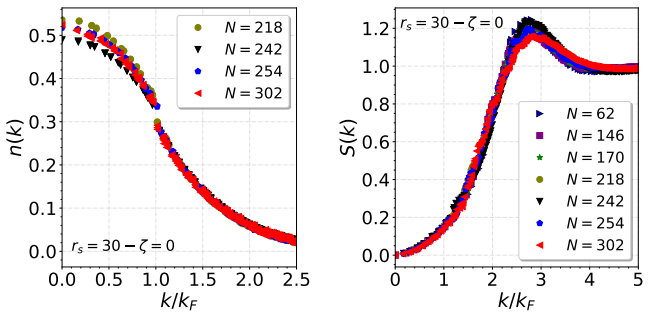

FIG. 2. Momentum density $n(k)$ and static structure factor $S(k)$ of paramagnetic two-dimensional uniform electron liquids using SJB WFs with density parameter $r_s = 30$ at different system sizes N obtained by VMC at zero twist. k_F is the Fermi wavevector.

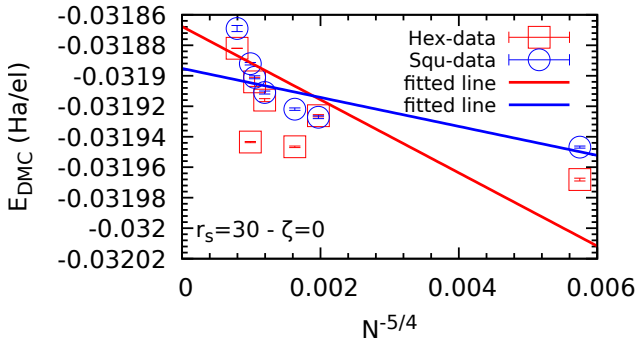

FIG. 3. Twist-averaged SJB-WF DMC energies of two-dimensional paramagnetic uniform electron liquids at $r_s = 30$ obtained using hexagonal and square simulation cells.

plotted the twist-averaged DMC energies as a function of $N^{-5/4}$ and used linear regression to obtain the DMC energy at the thermodynamic limit (Fig. 3). The DMC energies at the infinite system size limit obtained with hexagonal and square simulation cells are $-0.03187(2)$ and $-0.03189(1)$ Ha/el., respectively. The extrapolated results agree within the error bars; however, the fluctuations about the fitted lines are much larger than the error bars, so that we rely on fitting to multiple different system sizes to remove nonsystematic finite-size effects. The plot shows that the variation of the DMC energy as a function of system size N is smaller in the square lattice. The hexagonal Wigner crystal energies used in our phase diagram (Fig. 6) were calculated using hexagonal simulation cells.

Fifth, we performed SJ-VMC, SJ-DMC, and DMC with only the Slater trial WF (S-DMC) calculations for paramagnetic Fermi fluids at $r_s = 30$ in square cells with $N = 90$ electrons. We chose three different initial WFs for the optimization (Starting points 1–3) and optimized the Jastrow factor by energy minimization at either Γ ($\mathbf{k}_s = \mathbf{0}$) or the Baldereschi point [$\mathbf{k}_s = (1/4)\mathbf{b}_1 + (1/4)\mathbf{b}_2$, where $\mathbf{b}_1$ and $\mathbf{b}_2$ are the supercell reciprocal lattice vectors]. The DMC calculations were performed at time steps of 2 and 8 Ha^{-1}, with populations in inverse proportion to the time step, and the energies were extrapolated linearly to zero time step and infinite population. HF and VMC energies are shown in Table V, while DMC energies with and without a Jastrow factor are shown in Table VI.

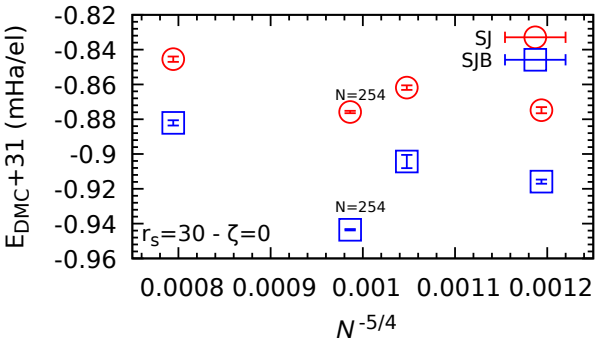

FIG. 4. TA DMC energies for paramagnetic ($\zeta = 0$) 2D UELs with density parameter $r_s = 30$ obtained using SJ and SJB WFs. The differences between the SJB and SJ energies for $N = 218$, 242, 254, and 302 are $-0.041(2)$, $-0.042(4)$, $-0.068(1)$, and $-0.037(2)$ mHa/el., respectively.

As expected, the choice of twist for optimization has only a small effect on the fluid energy at this low density. Indeed, twist averaging only has a small effect on the fluid energy. Starting points 2 and 3 produce WFs that give a significantly lower VMC energy than the HF energy, i.e., they introduce correlations that lower the energy. However, the energy obtained is not as low as the energy obtained in starting point 1. Hence there are issues with local minima in parameter space.

The S-DMC energy obtained with the HF WF is lower than the SJ-DMC energy obtained using the WFs from starting points 2 and 3, despite the fact that the HF energy is higher than the SJ-VMC energies. Hence these Jastrow factors introduce features that are difficult for DMC to remove (i.e., much smaller DMC time steps and longer simulations would be required). The S-DMC energy is in fairly good agreement with the SJ-DMC energy obtained with the good Jastrow factor obtained in starting point 1. The remaining small difference is very likely because of the need to extrapolate the S-DMC energy to zero time step more carefully. These findings confirm that our DMC results can be affected by trial wave functions whose variational parameters have not converged to the values that best describe the fluid ground state.

V. PHASE DIAGRAM

We calculated the TA DMC energy for all the system sizes shown in Fig. 1. The energy at the thermodynamic

TABLE IV. Optimized energy of paramagnetic 2D UELs at $r_s = 30$ with $N = 302$ electrons. Only polynomial and plane-wave two-body Jastrow terms were used. The energies were calculated using different numbers of configurations N_{conf}. Two different optimization methods, unreweighted variance minimization ("varmin") and MAD minimization ("madmin"), were used. Three twists, with fractional coordinates $\mathbf{k}_0 = (0,0)$, $\mathbf{k}_1 = (1/3,1/3)$, and $\mathbf{k}_2 = (1/4,1/2)$, were used. All the energies are in Ha/el. The energies which are lower than −0.031 Ha/el. are highlighted in bold.

N_{conf}	Twist $\mathbf{k}_0$		Twist $\mathbf{k}_1$		Twist $\mathbf{k}_2$	
	"varmin"	"madmin"	"varmin"	"madmin"	"varmin"	"madmin"
1920	−0.027955(7)	−0.019491(8)	−0.025725(2)	**−0.0315169(4)**	−0.025009(2)	**−0.0314244(5)**
3840	−0.019497(8)	−0.019508(8)	−0.028892(8)	−0.019487(9)	−0.0307900(8)	**−0.0315429(4)**
7680	−0.0307833(9)	**−0.0314710(4)**	−0.01950(1)	−0.019496(9)	−0.029414(3)	**−0.0315166(4)**
9600	−0.025907(2)	**−0.0315087(4)**	−0.019502(9)	−0.019496(8)	−0.028948(2)	−0.01948(1)
11520	−0.019503(8)	**−0.0315034(4)**	−0.030772(3)	**−0.0315255(4)**	−0.0308548(6)	−0.01949(1)
15360	−0.019492(8)	−0.019523(9)	**−0.0313126(5)**	−0.01948(2)	−0.030773(1)	−0.019507(9)
19200	−0.027983(2)	−0.019519(8)	−0.030738(2)	−0.019494(9)	−0.01947(1)	**−0.0315176(5)**

TABLE V. HF and SJ-VMC energies for 90-electron Fermi fluids in a square simulation cell, with the WF being optimized from three different random starting points at the Γ point and at the Baldereschi point of the square simulation cell.

$\mathbf{k}_s$	Start	Energy (Ha/el.)			
		HF	TA HF	SJ-VMC	TA SJ-VMC
Γ	1	−0.0196518	−0.0196034	−0.0317373(2)	−0.0317344(2)
Γ	2	−0.0196518	−0.0196034	−0.0251398(8)	−0.025177(2)
Γ	3	−0.0196518	−0.0196034	−0.0271506(7)	−0.02716(1)
Bald.	1	−0.0194515	−0.0196034	−0.0317356(2)	−0.0317350(2)
Bald.	2	−0.0194515	−0.0196034	−0.02495(1)	−0.02500(1)
Bald.	3	−0.0194515	−0.0196034	−0.0277466(6)	−0.027726(7)

TABLE VI. As Table V, but using S-DMC and SJ-DMC calculations.

$\mathbf{k}_s$	Start	Energy (Ha/el.)			
		S-DMC	TA S-DMC	SJ-DMC	TA SJ-DMC
Γ	1	−0.03151(2)	−0.03151(2)	−0.031919(1)	−0.031903(1)
Γ	2	−0.03151(2)	−0.03151(2)	−0.02676(7)	−0.02683(4)
Γ	3	−0.03151(2)	−0.03151(2)	−0.02848(2)	−0.02849(2)
Bald.	1	−0.03151(2)	−0.03159(2)	−0.031899(2)	−0.031898(1)
Bald.	2	−0.03151(2)	−0.03159(2)	−0.02670(2)	
Bald.	3	−0.03151(2)	−0.03159(2)	−0.02901(2)	−0.02901(2)

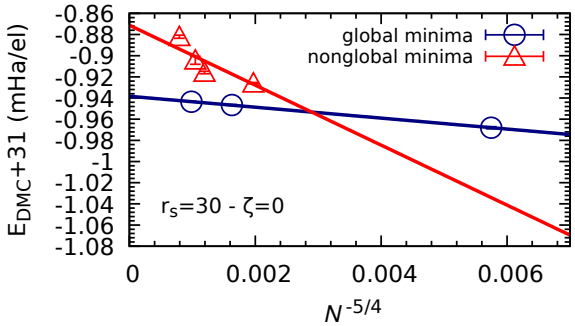

FIG. 5. Extrapolation of TA DMC fluid energies to the thermodynamic limit of infinite system size for paramagnetic ($\zeta = 0$) 2D UELs with density parameter $r_s = 30$. The red data points are assumed to be trapped in nonglobal minima during optimization and do not correspond to the fluid ground state.

limit is obtained by a linear extrapolation of the TA DMC energy as a function of $N^{-5/4}$ [29]. Figure 5 shows the extrapolation of TA DMC energies of two sets of data points labeled as "nonglobal minima" and "global minima." All the TA DMC energies at the infinite system size limit presented in the rest of this paper are obtained using the extrapolation of TA DMC of systems that we believe correspond to the fluid ground state.

Table VII lists our TA DMC energies at the thermodynamic limit for 2D UELs with spin polarizations $\zeta = 0$, 0.5, and 1, and density parameters $1 \le r_s \le 40$. We compare our results with the previous works of Drummond and Needs [28, 29]. The energies extrapolated to infinite system size are slightly lower than those obtained by Drummond and Needs. There are two major differences between our work and the previous ones. First, we used the two-body plane-wave backflow $\boldsymbol{\pi}$ term [50, 51], giving additional variational freedom in simulation cells of finite size. Second, we used larger system sizes and hexagonal simulation cells. These differences do not matter in principle, but in practice, they affect the extrapolation to infinite system size.

We used our DMC energies extrapolated to infinite system size to calculate the phase diagram of the 2D UEL (Fig. 6). The ferromagnetic and antiferromagnetic crystal energies used in our phase diagram calculation are taken from Ref. 28. We find that the paramagnetic Fermi fluid transitions to a hexagonal Wigner crystal at $r_s = 35(1)$. The previous work by Drummond and Needs [28] predicted a value of $r_s = 31(1)$ for this phase transition. Similar to the previous phase diagram [28], we find no region of stability for the polarized fluid phase with spin polarizations of $\zeta = 0.5$ or 1.

TABLE VII. DMC energy in Ha/el. in the infinite system-size limit for 2D UELs with spin polarizations $\zeta = 0$, 0.5, and 1 and density parameters $1 \le r_s \le 40$. The results of Drummond and Needs are taken from Refs. 28 and 29.

r_s	Present work			Drummond and Needs	
	$\zeta = 0$	$\zeta = 0.5$	$\zeta = 1$	$\zeta = 0$	$\zeta = 1$
1	−0.21017(6)	...	0.12626(4)	−0.2104(6)	...
2	−0.25846(7)	...	−0.19453(1)	...	...
5	−0.14998(2)	...	−0.143714(2)	−0.14963(3)	...
10	−0.085568(5)	...	−0.084585(6)	−0.085399(6)	...
15	−0.060138(2)	...	−0.059731(1)	...	...
20	−0.046388(1)	−0.0462813(1)	−0.046236(1)	−0.046305(4)	−0.046213(3)
25	−0.037807(3)	−0.0377575(1)	−0.037754(1)	−0.037774(2)	−0.037740(2)
30	−0.0319383(2)	−0.0319153(1)	−0.031919(2)	−0.031926(1)	−0.031913(1)
35	−0.0276718(4)	...	−0.027668(7)	−0.027665(1)	−0.027657(1)
40	−0.0244226(3)	...	−0.0244289(1)	−0.024416(1)	−0.024416(1)

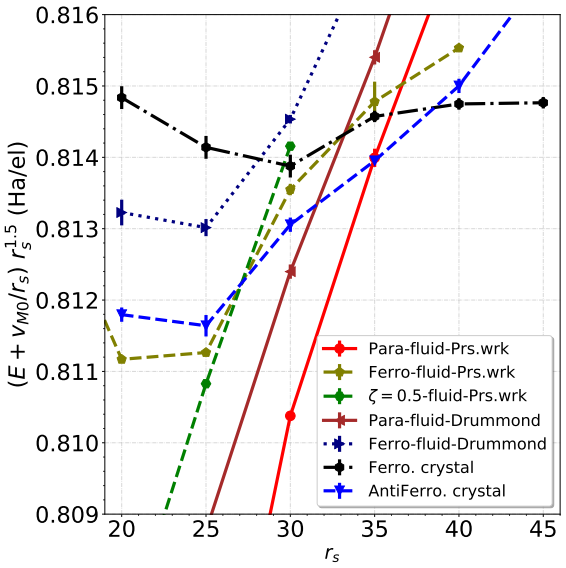

FIG. 6. DMC energy extrapolated to infinite system size as a function of r_s for 2D UELs with spin polarizations $\zeta = 0$, 0.5, and 1. Our results ("Prs-wrk") are compared with those of Drummond and Needs [28], which include paramagnetic ($\zeta = 0$) and ferromagnetic fluids ($\zeta = 1$), and ferromagnetic and antiferromagnetic hexagonal Wigner crystals. The Madelung energy of a hexagonal lattice, $-v_{M0}/r_s$, where $v_{M0} = -0.50751467391482663$ is the Madelung constant at $r_s = 1$, has been subtracted from all the DMC energies.

VI. CORRELATION ENERGY

The correlation energy E_c is given by the difference between the TA DMC energy at the thermodynamic limit and the HF energy. The HF energy of a 2D UEL in the infinite system size limit is

$$E_{HF}(r_s,\zeta) = \frac{1+\zeta^2}{2r_s^2} - \frac{2^{3/2}}{3r_s\pi}[(1+\zeta)^{3/2} + (1-\zeta)^{3/2}] \quad (1)$$

where $\zeta = (N_\uparrow - N_\downarrow)/N$ is the spin polarization. Our SJB-DMC correlation energy results are shown in Table VIII. We fit our TA DMC correlation energies to the Padé

TABLE VIII. SJB-DMC correlation energy in the limit of infinite system size for 2D UELs with spin polarizations $\zeta = 0$ and 1.

r_s	Correlation energy (Ha/el.)	
	$\zeta = 0$	$\zeta = 1$
1	−0.10996(6)	−0.02491(4)
2	−0.08335(7)	−0.02012(1)
5	−0.04993(2)	−0.013948(2)
10	−0.03054(5)	−0.009702(6)
15	−0.02235(2)	−0.007587(1)
20	−0.017627(1)	−0.006295(1)
25	−0.014598(3)	−0.005401(1)
30	−0.012487(2)	−0.004736(2)
35	−0.0109311(4)	−0.004232(7)
40	−0.0097298(3)	−0.0038332(1)

function [20]

$$E_c(r_s,\zeta) = a_\zeta \times \frac{1 + b_\zeta r_s^{1/2}}{1 + b_\zeta r_s^{1/2} + c_\zeta r_s + d_\zeta r_s^{3/2}}, \quad (2)$$

which has the correct asymptotic behavior at high and low densities [20], i.e., $E_c(r_s) = a - acr_s + O(r_s^{3/2})$ at small r_s, while $E_c(r_s \to \infty) = (ab/d)r_s^{-1} + a(1/d - bc/d^2)r_s^{-3/2} + O(r_s^{-2})$ at large r_s. We also fitted our DMC correlation energy data to the correlation function suggested by Rapisarda and Senatore [21]. For a given ζ the

correlation energy is written as

$$E_c(r_s) = a_0\Bigg\{1 + Ar_s\Bigg[B\ln\left(1 + a_1 r_s^{-1/2}\right) + \frac{C}{2}\ln\left(1 + 2a_2 r_s^{-1/2} + a_3 r_s^{-1}\right) + D\tan^{-1}\left(\frac{r_s^{1/2} + a_2}{\sqrt{a_3 - a_2^2}} - \frac{\pi}{2}\right)\Bigg]\Bigg\} \tag{3}$$

where

$$\begin{aligned} b &= a_1 + 2a_2 \qquad \text{and} \qquad b' = a_1 - 2a_2 \\ A &= \frac{2b}{2a_1a_2 - a_3 - a_1^2} \\ B &= \frac{1}{a_1} - \frac{1}{b} \\ C &= \frac{b'}{a_3} + \frac{1}{b} \\ D &= \frac{F - a_2 C}{\sqrt{a_3 - a_2^2}} \\ F &= 1 - b'\left(\frac{1}{b} - \frac{2a_2}{a_3}\right). \end{aligned} \tag{4}$$

The parameters a_0, a_1, a_2, and a_3 were determined by fitting. All the fitting parameters are listed in Table IX.

TABLE IX. Fitting parameters for the SJB-DMC correlation energy [Eq. (2)] of paramagnetic ($\zeta = 0$) and ferromagnetic ($\zeta = 1$) 2D UELs.

Parameter	$\zeta = 0$	$\zeta = 1$
	Padé	
a (Ha/el.)	−0.172202	−0.0428086
b	0.8729471	38.9315
c	0.7467841	22.4206
d	0.3135799	6.34817
	Rapisarda-Senatore	
a_0 (Ha/el.)	−0.184448	−0.044662
a_1	24.703763	−0.002965
a_2	0.0611422	1.8745574
a_3	3.7936341	11.327815

We plot our SJB-DMC data and the fitted functions in Fig. 7. The fitting parameter a in the Padé function and a_0 in the Rapisarda-Senatore function represents the correlation energy in the limit $r_s \to 0$. Within the random phase approximation (RPA) the correlation energy of paramagnetic 2D UEL is $E_c(r_s) = -(0.19 \pm 0.02) - 0.0863 r_s \ln(r_s) + O(r_s)$ in Ha/el. [16]. The existence of $\ln(r_s)$ indicates that the correlation energy is a nonanalytical function of r_s for $r_s \to 0$. The first term in the RPA approximation $-(0.19 \pm 0.02)$ is comparable with our fitting parameters of a in the Padé function and a_0 in the Rapisarda-Senatore function for the paramagnetic case. However, RPA approximation of the asymptotic term is unknown for the spin-polarized 2D UEL and one has to rely on the fitting parameters. We found that both fitting functions we used provide a close estimation of correlation energy of fully spin-polarized 2D electron liquid in the limit of $r_s \to 0$, as listed in Table IX.

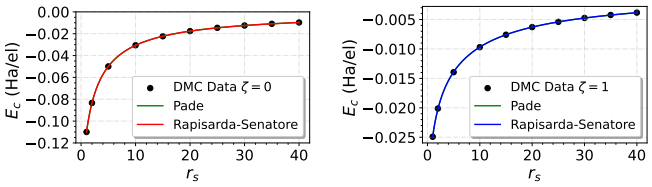

FIG. 7. DMC correlation energy of 2D uniform electron liquid with $\zeta = 0$ (left panel) and spin polarization $\zeta = 1$ (right panel) fitted by Padé and Rapisarda and Senatore [21] functions. The fitting parameters are listed in Table IX. Both fitted functions provide similar asymptotic behavior.

VII. CONCLUSION

In summary, we have used SJB WFs to perform VMC and DMC calculations for 2D UELs with spin polarizations $\zeta = 0$, 0.5, and 1 within the density range $1 \le r_s \le 40$. We have corrected single-particle and many-body FS errors by canonical-ensemble TA and extrapolation of the TA energies to infinite system size. We find that separately optimizing the Jastrow factor and backflow function at each twist improves the TA DMC energy for the density range $1 \le r_s \le 5$ and possibly beyond. Optimization of the trial WF is challenging near the transition density because the complexity of the energy landscape makes it difficult to find the ground state corresponding to the Fermi fluid. We predict that the paramagnetic 2D UEL transforms to a Wigner crystal at $r_s = 35(1)$. We have not found any region of stability for 2D UELs with spin polarizations $\zeta = 0.5$ or 1.

ACKNOWLEDGMENTS

S.A. and S.M.V. acknowledge support from the UK EPSRC grants EP/P015794/1 and EP/W010097/1, the Royal Society, and the Advanced Research Computing (ARC) service of the University of Oxford.

[1] D. Pines and P. Noziéres, *The Theory of Quantum Liquids* (W.A. Benjamin, Inc., New York, 1966).

[2] P.-F. Loos and P. M. W. Gill, Wiley Interdiscip. Rev.: Comput. Mol. Sci. **6**, 410 (2016).

[3] R. M. Dreizler and E. K. U. Gross, *Density Functional Theory* (Springer-Verlag: Berlin, 1990).
[4] P. Hohenberg and W. Kohn, Phys. Rev. **136**, B864 (1964).
[5] W. Kohn and L. J. Sham, Phys. Rev. **140**, A1133 (1965).
[6] L. D. Landau, J. Expt. Theor. Phys. (USSR) **35**, 97 (1958).
[7] J. M. Luttinger, Phys. Rev. **121**, 942 (1961).
[8] G. Senatore and N. H. March, Rev. Mod. Phys. 66, 445 **66**, 455 (1994).
[9] T. Dornheim, S. Groth, T. Sjostrom, F. D. Malone, W. M. C. Foulkes, and M. Bonitz, Phys. Rev. Lett. **117**, 156403 (2016).
[10] T. Dornheim, S. Groth, and M. Bonitz, Phys. Rep. **744**, 1 (2018).
[11] S. H. Vosko, L. Wilk, and M. Nusair, Can. J. Phys. **58**, 1200 (1980).
[12] J. P. Perdew and Y. Wang, Phys. Rev. B **45**, 13244 (1992).
[13] P. Bhattarai, A. Patra, C. Shahi, and J. P. Perdew, Phys. Rev. B **97**, 195128 (2018).
[14] E. P. Wigner, Phys. Rev. **46**, 1002 (1934).
[15] F. Bloch, Z. Phys. **57**, 545 (1929).
[16] G. Giuliani and G. Vignale, *Quantum Theory of the Electron Liquid* (Cambridge University Press, Cambridge, UK, 2005).
[17] D. M. Ceperley, G. V. Chester, and M. H. Kalos, Phys. Rev. B **16**, 3081 (1977).
[18] D. M. Ceperley, Phys. Rev. B **18**, 3126 (1978).
[19] D. M. Ceperley and B. J. Alder, Phys. Rev. Lett. **45**, 566 (1980).
[20] B. Tanatar and D. M. Ceperley, Phys. Rev. B **39**, 5005 (1989).
[21] F. Rapisarda and G. Senatore, Aust. J. Phys. **49**, 161 (1996).
[22] G. Cassella, H. Sutterud, S. Azadi, N. Drummond, D. Pfau, J. Spencer, and W. Foulkes, Phys. Rev. Lett. **130**, 036401 (2023).
[23] J. Hermann, J. Spencer, K. Choo, A. Mezzacapo, W. Foulkes, D. Pfau, G. Carleo, and F. Noé', Nat. Rev. Chem. **7**, 692 (2023).
[24] P. Gori-Giorgi, S. Moroni, and G. B. Bachelet, Phys. Rev. B **70**, 115102 (2004).
[25] S. D. Palo, M. Botti, S. Moroni, and G. Senatore, Phys. Rev. Lett. **94**, 226405 (2005).
[26] D. Varsano, S. Moroni, and G. Senatore, Europhys. Lett. **53**, 348 (2001).
[27] C. Attaccalite, S. Moroni, P. Gori-Giorgi, and G. B. Bachelet, Phys. Rev. Lett. **88**, 256601 (2002).
[28] N. D. Drummond and R. J. Needs, Phys. Rev. Lett. **102**, 126402 (2009).
[29] N. D. Drummond and R. J. Needs, Phys. Rev. B **79**, 085414 (2009).
[30] T. Ando, A. B. Fowler, and F. Stern, Rev. Mod. Phys. **54**, 437 (1982).
[31] P. Phillips, Y. Wan, I. Martin, S. Knysh, and D. Dalidovich, Nature **395**, 253 (1998).
[32] J. Davies, *The Physics of Low-Dimensional Semiconductors* (Cambridge University Press, 1997).
[33] S. Datta, *Electronic Transport in Mesoscopic Systems* (Cambridge University Press, 1995).
[34] J. Falson, I. Sodemann, B. Skinner, D. Tabrea, Y. Kozuka, A. Tsukazaki, M. Kawasaki, K. von Klitzing, and J. H. Smet, Nat. Mat. **21**, 311 (2022).
[35] A. Ghosh, C. J. B. Ford, M. Pepper, H. E. Beere, and D. A. Ritchie, Phys. Rev. Lett. **92**, 116601 (2004).
[36] C. C. Grimes and G. Adams, Phys. Rev. Lett. **42**, 795 (1979).
[37] E. Y. Andrei, G. Deville, D. C. Glattli, F. I. B. Williams, E. Paris, and B. Etienne, Phys. Rev. Lett. **60**, 2765 (1988).
[38] V. J. Goldman, M. Santos, M. Shayegan, and J. E. Cunningham, Phys. Rev. Lett. **65**, 2189 (1990).
[39] H. C. Manoharan, Y. W. Suen, M. B. Santos, and M. Shayegan, Phys. Rev. Lett. **77**, 1813 (1996).
[40] M. Hossain, T. Zhao, S. Pu, M. A. Mueed, M. K. Ma, K. A. V. Rosales, Y. J. Chung, L. N. Pfeiffer, K. W. West, K. W. Baldwin, J. K. Jain, and M. Shayegan, Nat. Phys. **17**, 48 (2021).
[41] P. Madathil, C. Wang, S. Singh, A. Gupta, K. V. Rosales, Y. Chung, K. West, K. Baldwin, L. Pfeiffer, L. Engel, and M. Shayegan, Phys. Rev. Lett. **132**, 096502 (2024).
[42] M. Shayegan, Nat. Rev. Phys. **4**, 212 (2022).
[43] S. Chiesa, D. M. Ceperley, R. M. Martin, and M. Holzmann, Phys. Rev. Lett. **97**, 076404 (2006).
[44] N. D. Drummond, R. J. Needs, A. Sorouri, and W. M. C. Foulkes, Phys. Rev. B **78**, 125106 (2008).
[45] M. Holzmann, R. C. Clay, III, M. A. Morales, N. M. Tubman, D. M. Ceperley, and C. Pierleoni, Phys. Rev. B **94**, 035126 (2016).
[46] P. R. C. Kent, R. Q. Hood, A. J. Williamson, R. J. Needs, W. M. C. Foulkes, and G. Rajagopal, Phys. Rev. B **59**, 1917 (1999).
[47] C. Lin, F. H. Zong, and D. M. Ceperley, Phys. Rev. E **64**, 016702 (2001).
[48] P. López Ríos, A. Ma, N. D. Drummond, M. D. Towler, and R. J. Needs, Phys. Rev. E **74**, 066701 (2006).
[49] N. D. Drummond, M. D. Towler, and R. J. Needs, Phys. Rev. B **70**, 235119 (2004).
[50] S. Azadi, N. Drummond, and S. M. Vinko, Phys. Rev. B **108**, 115134 (2023).
[51] S. Azadi, N. D. Drummond, and S. M. Vinko, Phys. Rev. B **107**, L121105 (2023).
[52] S. Azadi and N. D. Drummond, Phys. Rev. B **105**, 245135 (2022).
[53] W. M. C. Foulkes, L. Mitas, R. J. Needs, and G. Rajagopal, Rev. Mod. Phys. **73**, 33 (2001).
[54] R. J. Needs, M. D. Towler, N. D. Drummond, P. López Ríos, and J. R. Trail, J. Chem. Phys. **152**, 154106 (2020).
[55] J. B. Anderson, J. Chem. Phys. **65**, 4121 (1976).
[56] C. J. Umrigar, K. G. Wilson, and J. W. Wilkins, Phys. Rev. Lett. **60**, 1719 (1988).
[57] N. D. Drummond and R. J. Needs, Phys. Rev. B **72**, 085124 (2005).
[58] D. Bressanini, G. Morosi, and M. Mella, J. Chem. Phys. **116**, 5345 (2002).
[59] C. J. Umrigar, J. Toulouse, C. Filippi, S. Sorella, and R. G. Hennig, Phys. Rev. Lett. **98**, 110201 (2007).